How Photogenerated I$_2$ Induces I-Rich Phase Formation in Lead Mixed Halide Perovskites

Yang Zhou,* Simone C. W. van Laar, Daniele Meggiolaro,* Luca Gregori,
Samuele Martani, Jia-Yong Heng, Kunal Datta, Jesús Jiménez-López, Feng Wang,
E Laine Wong, Isabella Poli, Antonella Treglia, Daniele Cortecchia, Mirko Prato,
Libor Kobera, Feng Gao, Ni Zhao, René A. J. Janssen, Filippo De Angelis,
and Annamaria Petrozza*

Bandgap tunability of lead mixed halide perovskites (LMHPs) is a crucial characteristic for versatile optoelectronic applications. Nevertheless, LMHPs show the formation of iodide-rich (I-rich) phase under illumination, which destabilizes the semiconductor bandgap and impedes their exploitation. Here, it is shown that how I$_2$, photogenerated upon charge carrier trapping at iodine interstitials in LMHPs, can promote the formation of I-rich phase. I$_2$ can react with bromide (Br$^-$) in the perovskite to form a trihalide ion I$_2$Br$^-$ (I$^{\delta-}$-I$^{\delta+}$-Br$^{\delta-}$), whose negatively charged iodide (I$^{\delta-}$) can further exchange with another lattice Br$^-$ to form the I-rich phase. Importantly, it is observed that the effectiveness of the process is dependent on the overall stability of the crystalline perovskite structure. Therefore, the bandgap instability in LMHPs is governed by two factors, i.e., the density of native defects leading to I$_2$ production and the Br$^-$ binding strength within the crystalline unit. Eventually, this study provides rules for the design of chemical composition in LMHPs to reach their full potential for optoelectronic devices.

1. Introduction

Lead halide perovskites (LHPs, chemical formula APbX$_3$, A = formamidinium (FA$^+$), methylammonium (MA$^+$), or Cs$^+$ and X = I$^-$, Br$^-$, or Cl$^-$) have demonstrated their potential as a material platform for a new generation of optoelectronic technology. One superior feature of LHPs is their continuously tunable bandgap from near infrared to ultraviolet by substituting I$^-$ with Br$^-$ and Cl$^-$ at the X-site through simple solution processing.[1] This enables LHPs to provide top absorbers with matched bandgaps for tandem solar cells[2] and emissive layers for colorful light-emitting diodes (LEDs),[3] just to mention the most common applications. However, the bandgap tunability of LHPs cannot be practically attained

Y. Zhou, S. Martani, J. Jiménez-López, E L. Wong, I. Poli, A. Treglia,
D. Cortecchia, A. Petrozza
Center for Nano Science and Technology@Polimi
Istituto Italiano di Tecnologia
via Rubattino 81, Milano 20134, Italy
E-mail: yang.zhou@iit.it; annamaria.petrozza@iit.it
S. C. W. van Laar, K. Datta, R. A. J. Janssen
Molecular Materials and Nanosystems
Institute for Complex Molecular Systems
Eindhoven University of Technology
P.O. Box 513, Eindhoven 5600 MB, The Netherlands

The ORCID identification number(s) for the author(s) of this article can be found under https://doi.org/10.1002/adma.202305567

D. Meggiolaro, L. Gregori, F. De Angelis
Computational Laboratory for Hybrid/Organic Photovoltaics (CLHYO)
Istituto CNR di Scienze e Tecnologie Chimiche "'Giulio Natta'"
(CNR-SCITEC)
Via Elce di Sotto 8, Perugia 06123, Italy
E-mail: daniele.meggiolaro@cnr.it
L. Gregori, F. De Angelis
Department of Chemistry
Biology and Biotechnology
University of Perugia and INSTM
Via Elce di Sotto 8, Perugia 06123, Italy
J.-Y. Heng, N. Zhao
Electronic Engineering Department
The Chinese University of Hong Kong
Shatin, NT 999077, Hong Kong
F. Wang, F. Gao
Department of Physics
Chemistry and Biology
Linköping University
Linköping SE-58183, Sweden

because of the I-rich phase formation under illumination.[4] The I-rich phase acts as charge carrier funneling center, reducing the performance of solar cells[5] and redshifting the emission in LEDs.[6] To reach the full potential of LHPs in optoelectronic applications, it is indispensable that the fundamentals behind the photoinstability are comprehensively understood.

Since the first report,[4] multiple models have been proposed to explain the processes behind light-induced I-rich phase formation, whereas no one to date fully rationalizes the diverse observations upon such phenomenon and its origin is still under debate. In mixed-halide perovskites $APb(I_{1-x}Br_x)_3$, it has been shown that the formed I-rich phase has a specific Br-fraction x of ≈ 0.2[4] under illumination. This is explained by thermodynamically favored phase segregation following a phase diagram and possibly roots in the escalated strain due to preferential anion lattice spacings[7] or electron-phonon coupling[8] under illumination. The phase diagram was further reconstructed by coupling the presence of photo-generated carrier with thermodynamical modeling.[9] The strain-based models are supported by the suppressed I-rich phase formation by incorporating Cs^+ at A-site, which is suggested to weaken lattice polaron formation[10] or static microstrain.[11] However, these models indicate a temperature-dependent Br-fraction in the formed I-rich phase, while a recent study shows x having little to no temperature dependence which suggests a thermodynamic bandgap-based model.[10a,12]

The role of defect activity in light-induced I-rich phase formation is gaining more and more consensus. Multiple reports suggest that local electrical field created by photocarrier trapping[5a,13] or strong photocarrier gradient[14] could cause unbalanced halide migration and I-rich phase formation under illumination. Halide vacancies are likely to provide the primary halide migration pathway.[13d,15] Pure-iodide lead perovskite has shown enhanced ionic conductivity under illumination, which is attributed to the increased iodide vacancies formed through I^- oxidation by photocarriers.[16] Furthermore, it has been shown that in mixed I-Br perovskites, photoexcitation boosts the transportation of I^- rather than Br^-, since I^- has lower oxidation potential and its vacancies are mainly generated.[17]

It is now well accepted that I_2 is one of the main products upon photocarrier trapping in tri-iodide lead perovskite[18] and contributes to its photo-degradation.[19] Recently, we demonstrated that the formation of I-rich phase in mixed I-Br perovskites is closely correlated with the carrier trapping at interstitial iodide defects and the formation of I_2, thus indicating that photo-degradation in tri-iodide and bandgap instability in mixed I-Br perovskites may have the same root.[20] Here, we show how the

photogenerated I_2 induces the I-rich phase formation in mixed I-Br perovskites. To rationalize the mechanism, we exposed mixed I-Br and pure-Br perovskites to I_2 vapor in the dark; both materials show the formation of I-rich phase after I_2 treatment. Through combined optical spectroscopies, X-ray diffraction (XRD), X-ray photoelectron spectroscopy (XPS) analyses and computational studies, we propose that I_2 react with Br^- to form the intermediate triple halide ion I_2Br^- ($I^{\delta-}$-$I^{\delta+}$-$Br^{\delta-}$), which leads to I^- formation through a series of chemical reactions, and thus increases the local I^- to Br^- ratio in the perovskite. Our model rationalizes how the prominence of I_2 formation under illumination, and binding strength of Br^- with respect to its ability to react with I_2 regulate the formation of I_2Br^- and I-rich phase, providing the guidance for achieving photostable mixed I-Br perovskites and devices.

2. Results and Discussion

2.1. Impact of I_2 Exposure on Lead Mixed I-Br and Pure-Br Perovskites

$Cs_{0.17}FA_{0.83}PbI_{1.5}Br_{1.5}$ perovskite with a bandgap of 1.85 eV was first used as a model material for our study.[2,21] The thin film was prepared by an anti-solvent method[22] (details provided in Experimental Section). We first checked the photo-induced I_2 formation by immersing the $Cs_{0.17}FA_{0.83}PbI_{1.5}Br_{1.5}$ thin film in anhydrous toluene under a white LED with intensity calibrated to 1 sun at 30 °C. The evolution of I_2 formation is monitored by measuring the ultraviolet-visible (UV–Vis) absorption of the anhydrous toluene in contact with the perovskite film.[19b] **Figure 1** shows the schematic of the I_2 formation experiment. As shown in Figure 1b, the I_2 absorption signal is detected in toluene after light soaking and becomes more intense with longer soaking time (up to 3 h), which indicates the I_2 formation in the $Cs_{0.17}FA_{0.83}PbI_{1.5}Br_{1.5}$ perovskite. A recent study from Martani et al. shows a correlation between I-rich phase formation under illumination and I_2 generation through charge carriers trapping at iodide interstitials.[20] The latter is accompanied by the increase of iodide vacancies.[13d,15,16] Thus, to investigate the sole effect of I_2 on altering optical and structural properties without increasing iodide vacancies[13d,15,16] in the mixed I-Br perovskite, we exposed the $Cs_{0.17}FA_{0.83}PbI_{1.5}Br_{1.5}$ perovskite to I_2 vapor in the dark. Note that I_2 treatment was performed in a N_2-filled glovebox. Figure 1c shows a schematic of the experiment, during which the I_2 beads were heated at 50 °C as the source of I_2 vapor and the sample was kept at room temperature (RT). The pristine film shows a photoluminescence (PL) emission at 670 nm. Following I_2 vapor exposure, the PL peak broadens and redshifts to 702 and 744 nm after 20 and 40 min, respectively (Figure 1d). Meanwhile, the onset of UV–Vis absorption spectrum redshifts and flattens upon I_2 exposure (Figure 1e). These results indicate that I_2 treatment induces the formation of I-rich phase with high energetic disorder. The X-ray diffraction pattern (XRD) of the pristine perovskite shows two main peaks at 14.40° and 29.02° which correspond to the (100) and (200) planes of a cubic lattice, respectively (Figure 1f).[1b] Over 40 min of I_2 exposure, the (200) diffraction peak shifts to lower angle and widens, but with a negligible growth at the high-angle tail (inset of Figure 1f). This demonstrates the overall expansion of the perovskite lattice with increased structural disorder.

M. Prato
Materials Characterization Facility
Istituto Italiano di Tecnologia
Via Morego, Genova 16163, Italy

L. Kobera
Institute of Macromolecular Chemistry
Czech Academy of Sciences
Heyrovsky Sq. 2, Prague 6 162 06, Czech Republic

F. De Angelis
SKKU Institute of Energy Science and Technology (SIEST)
Sungkyunkwan University
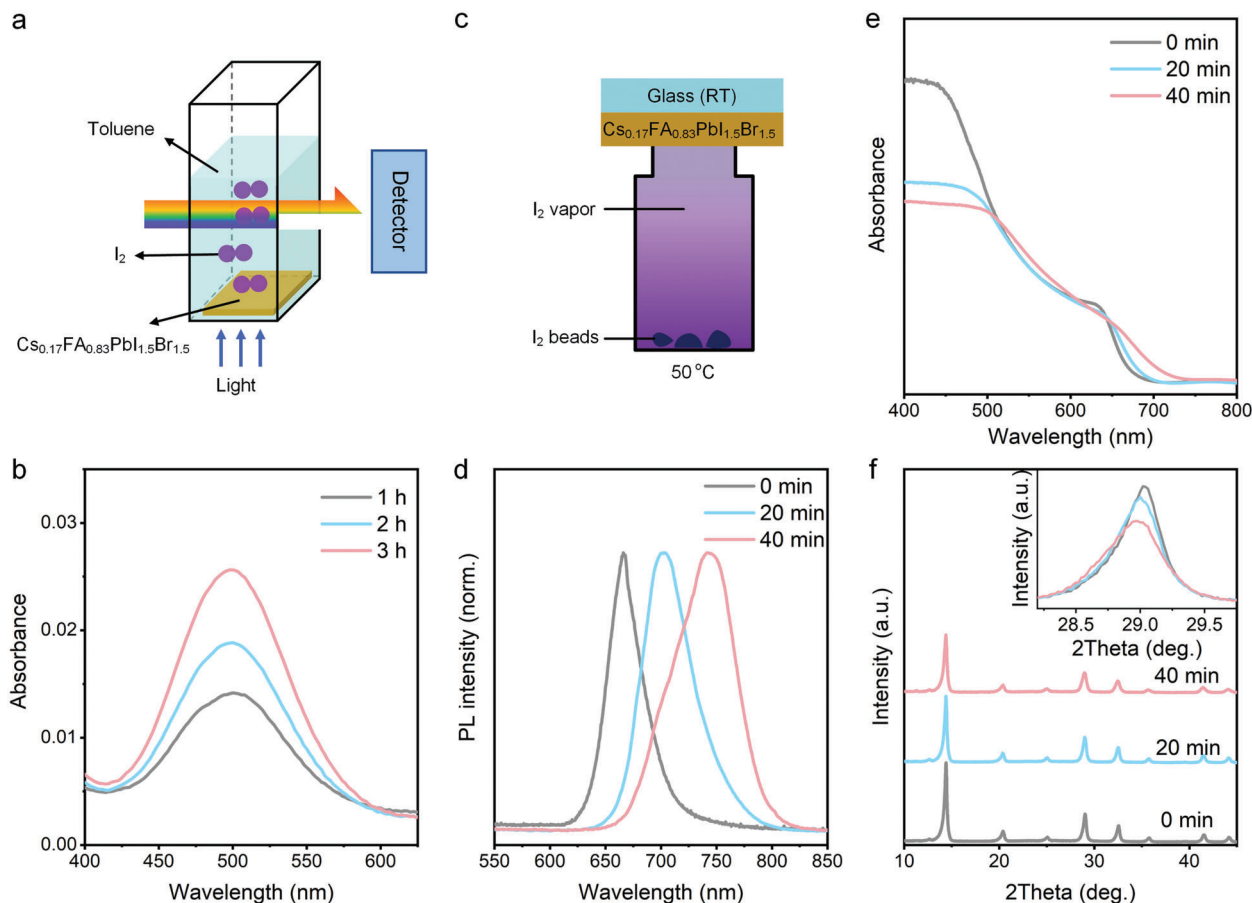Suwon 440–746, South Korea

**ADVANCED
SCIENCE NEWS**

www.advancedsciencenews.com

**ADVANCED
MATERIALS**

www.advmat.de

Figure 1. a) Schematic of monitoring I_2 formation in $Cs_{0.17}FA_{0.83}PbI_{1.5}Br_{1.5}$ perovskite under illumination (a white light LED with an intensity of 100 mW cm^{-2}). The thin film sample is placed in toluene and the I_2 signal in toluene is measured by absorption spectroscopy. b) Evolution of I_2 formation in $Cs_{0.17}FA_{0.83}PbI_{1.5}Br_{1.5}$ thin film under illumination over 3 h. c) Schematic of I_2 vapor exposure to the $Cs_{0.17}FA_{0.83}PbI_{1.5}Br_{1.5}$ thin film in the dark and in the N_2-filled glovebox. The sample is kept at room temperature (RT). d) PL spectra, e) UV–Vis absorption spectra and f) XRD patterns of $Cs_{0.17}FA_{0.83}PbI_{1.5}Br_{1.5}$ perovskite upon I_2-vapor exposure in the dark over 40 min.

Combined with PL and absorption results (Figures 1d,e), the lattice expansion observed in the perovskite exposed to I_2 can be attributed to the overall enrichment of I$^-$ in the lattice. Since the I$^-$ ratio in the perovskite lattice directly relates to the XRD peak position,[1b] we can estimate that the average I$^-$ ratio y ($y = 1-x$, x is Br$^-$ ratio) is increased by 0.008 and 0.018 upon I_2 vapor exposure for 20 and 40 min, respectively (Figure S1 and Table S1, Supporting Information). The detail of the estimation is given on page 4 in Supporting Information. The enrichment of I$^-$ in the perovskite lattice requires extra I$^-$ and implies I_2 being the I$^-$ source.

To confirm that the extra I$^-$ enriching the $Cs_{0.17}FA_{0.83}PbI_{1.5}Br_{1.5}$ perovskite lattice is produced by I_2, we further tested I_2 exposure on the pure-Br perovskite of $Cs_{0.17}FA_{0.83}PbBr_3$. The pristine sample shows a PL emission at 550 nm (**Figure 2**a). After exposure to I_2 vapor for 20 min, we observe the emergence of a broad band peaking at ≈705 nm (Figure 2a). This implies the formation of the I-rich phase with a broad I$^-$ to Br$^-$ distribution. X-ray photoelectron spectroscopy (XPS) was further conducted for elemental analysis. The spectra of I $3d$ are shown in Figure 2b and those of the other elements in the perovskite are given in Figure S2 (Supporting Information).

The pristine sample does not show any signal from the iodine species according to the XPS spectrum (Figure 2b), while after I_2 treatment a weak XPS peak of I $3d_{5/2}$ emerges at a binding energy of (619.0 ± 0.2) eV (Table S2, Supporting Information). This should be assigned to I$^-$ but not I_2, since I $3d_{5/2}$ of I_2 is at ≈620 eV.[23] This confirms that I_2 can be converted to I$^-$ when in contact with the perovskite, which can further incorporate into the lattice. The concentration of I$^-$ in the I_2-treated $Cs_{0.17}FA_{0.83}PbBr_3$ perovskite is quantified based on the XPS spectrum with a value of 0.3 at% (Table S3, Supporting Information). Though this indicates that the formed I-rich phase in the $Cs_{0.17}FA_{0.83}PbBr_3$ perovskite after I_2 exposure may be in a small quantity, it is still able to act as charge funneling center and redshift the PL emission.[5b]

2.2. Mechanism behind I_2 Induced I-Rich Phase Formation

We further investigated the possible process of converting I_2 to I$^-$ when I_2 is in contact with Br-containing perovskite. We exclude the possibility of I$^-$ formation through the oxidation of Br$^-$ by I_2, because of the much higher oxidation potential of Br$^-$ (1.07 V) than that of I$^-$ (0.53 V) (see the analysis in Supporting
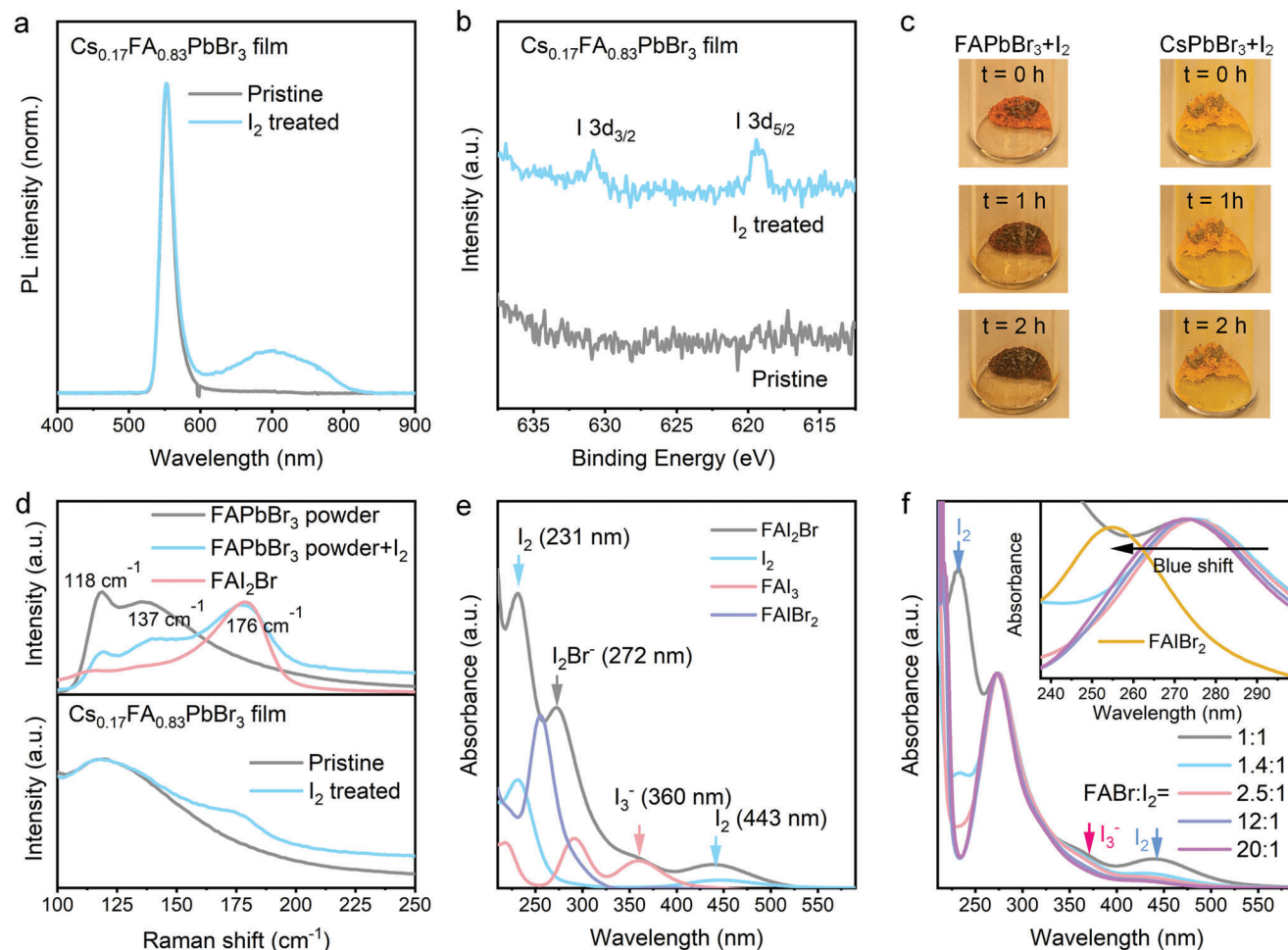
Figure 2. a) PL and b) XPS spectra of the $Cs_{0.17}FA_{0.83}PbBr_3$ before and after 20 min I_2 vapor exposure. c) Photo images of the $FAPbBr_3$-I_2 and $CsPbBr_3$-I_2 mixtures over 2 h. d) Raman spectra of $FAPbBr_3$ powder and $FAPbBr_3$-I_2 mixture after 2 h mixing. The Raman spectrum of FAI_2Br is given for reference. e) Raman spectra of $Cs_{0.17}FA_{0.83}PbBr_3$ perovskite thin films before and after I_2 exposure. f) UV–Vis absorption spectra of FAI_2Br, FAI_3, $FAIBr_2$, and I_2 dissolved in ethanol. FAI_2Br, FAI_3 and $FAIBr_2$ are prepared by mixing FABr with I_2, FAI with I_2, and FABr with IBr in a mole ratio of 1 : 1, respectively. g) UV–Vis absorption spectra of FABr-I_2 mixtures in ethanol by varying FABr to I_2 mole ratio from 1:1 to 20:1. The inset shows the blueshift of the absorption feature of I_2Br^- by increasing the FABr to I_2 ratio.

Information). I_2 is a well-known electron acceptor in the presence of ionic halide electron donors like Br^-, forming a wide variety of triple halide species including I_2Br^-,[24] during which the neutral iodine (I^0) becomes partially positively and negatively charged in I_2Br^- ($I^{\delta-}$-$I^{\delta+}$-$Br^{\delta-}$)[25]:

$$Br^- + I_2 \rightleftharpoons I_2Br^- \tag{1}$$
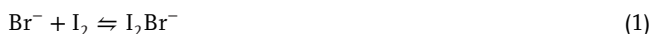
The charge density of the cation bonded with halide ions affects their ability of donating electrons and thus the ability to form triple halide ions with I_2.[26] We first checked the feasibility of I_2Br^- formation in a pure FA, a pure Cs and a mixed Cs-FA environment by mixing FABr, CsBr, and I_2 in a molar ratio of (1: 0: 1), (0: 1: 1) and (0.17: 0.83: 1) at a temperature of 25 °C, respectively. It is shown that in the two environments containing FA, the mixtures of bromide salts and I_2 show prominent reaction to form a dark red compound, while no visible reaction can be observed in the pure-Cs environment (Figure S3a, Supporting In-

formation). Polyhalides typically yield intense Raman signals due to the large polarizability of their electron-rich structures[27]; thus, we exploited this technique to probe their formation. The Raman spectrum of the compound formed in the FA-containing environments matches that of the I_2Br^- ion (Figures S3b,c, Supporting Information),[27] suggesting its formation in this scenario. With the presence of Cs^+, the formation of the I_2Br^- ion is suppressed and is possibly due to higher charge density (smaller radius) of Cs^+ than FA^+ (Figure S3a, Supporting Information), which binds Br^- more tightly and increases the negative charge localization near the cation, and thus weakens the capability of Br^- to polarize I_2 to form the triple halide ion.[26]

We further synthesized $FAPbBr_3$ and $CsPbBr_3$ powders and mixed them separately with I_2 in a molar ratio of 1:1 to check their feasibility of reacting with I_2. Over a period of 2 h, the $FAPbBr_3$-I_2 mixture shows prominent change in color, while that of $CsPbBr_3$-I_2 mixture shows no visible change (Figure 2c). Raman measurement was also conducted on the $FAPbBr_3$ powder

**ADVANCED
SCIENCE NEWS**

www.advancedsciencenews.com

**ADVANCED
MATERIALS**

www.advmat.de

and FAPbBr$_3$-I$_2$ mixture (after 2 h mixing), to elucidate the reaction happening behind the color change. As shown in Figure 2d, the FAPbBr$_3$ powder shows two peaks at 118 and 137 cm^{-1}, which are assigned to the coupled modes between the organic cation motion influenced by the inorganic octahedral (Figure 2d).[28] After mixing with I$_2$, one additional vibration mode centered at 176 cm^{-1} appears in the spectrum, which indicates the formation of I$_2$Br$^-$ [27] (The Raman spectra of FAI$_2$Br is given as a reference, Figure 2d). In the CsPbBr$_3$-I$_2$ mixture no I$_2$Br$^-$ can be detected by Raman spectroscopy (Figure S4, Supporting Information), indicating the suppression of the triple halide formation compared with the FA counterpart. The different reactivity of FAPbBr$_3$ and CsPbBr$_3$ with I$_2$ to form I$_2$Br$^-$ support the role of the A-site cation in the process.

Based on these results, we further elucidate the processes that are occurring when Cs$_{0.17}$FA$_{0.83}$PbBr$_3$ thin film is exposed to I$_2$ vapor. Raman spectra of the Cs$_{0.17}$FA$_{0.83}$PbBr$_3$ thin film before and after I$_2$ vapor exposure were measured. Compared with FAPbBr$_3$, the two peaks of 118 and 137 cm^{-1} merges into a broad peak in the spectrum of pristine Cs$_{0.17}$FA$_{0.83}$PbBr$_3$ (Figure 2e), which is possibly due to the incorporation of Cs at A-site affecting the coupled modes between the organic cation motion. In addition, the Raman feature of I$_2$Br$^-$ at 176 cm^{-1} arises after I$_2$ vapor exposure, which indicates the formation of I$_2$Br$^-$ (Figure 2e).

It has been reported that I$_2$Br$^-$ can further produce IBr$_2^-$ (Br$^{\delta-}$-I$^{\delta+}$-Br$^{\delta-}$)[25] and I$^-$ by reacting with another Br$^-$[29]:

$$I_2Br^- + Br^- \leftrightarrows IBr_2^- + I^- \tag{2}$$

To confirm this, we dissolved FAI$_2$Br in ethanol, and measured the absorption by UV–Vis spectroscopy. The absorption spectra of I$_2$, FAI$_3$ and FAIBr$_2$ dissolved in ethanol were also measured as references. FAI$_3$ and FAIBr$_2$ were prepared by mixing FAI with I$_2$ and FABr with IBr in a molar ratio of 1:1, respectively. The absorption spectrum of FAI$_2$Br shows peaks at 231, 272, 360, and 443 nm (Figure 2f). The peak at 272 nm indicates the formation I$_2$Br$^-$ (Figure 2f).[29] Peaks at 231 and 443 nm belongs to I$_2$ (Figure 2f), and indicates the conversion of Br$^-$ and I$_2$ to I$_2$Br$^-$ is incomplete. In addition, the peak at 360 nm is assigned to I$_3^-$ (Figure 2f), which indicates the existence of I$^-$ ions in the solution and they can combine with residual I$_2$ to form I$_3^-$:

$$I^- + I_2 \leftrightarrows I_3^- \tag{3}$$

Therefore, this confirms that I$^-$ can be produced through Rxn. 2. Through the available thermodynamic data, the reaction constant K of Rxn. 2 at 25 °C can be further obtained[29,30]:

$$K = \frac{(IBr_2^-)(I^-)}{(I_2Br^-)(Br^-)} = 1.4 \times 10^{-4} \tag{4}$$

As such, the concentration of formed IBr$_2^-$ may be much lower than that of I$_2$Br$^-$, whose absorption feature (at 255 nm shown in Figure 2f) may be buried under that of I$_2$Br$^-$. Extra FABr is further introduced in the solution of FAI$_2$Br to verify the Rxns. 1–3. By increasing FABr to I$_2$ ratio from 1:1 to 20:1, the absorption feature of I$_2$Br$^-$ shows a blueshift (inset of Figure 2g) toward that of IBr$_2^-$ at 255 nm, which indicates the increase of IBr$_2^-$ concentration and confirms the occurrence of Rxn. 2.[29]

Meanwhile, the signals of both I$_2$ and I$_3^-$ diminishes upon increasing of Br$^-$ (Figure 2g), confirming the consumption of I$_2$ to form more I$_2$Br$^-$ (Rxn. 1) and also the suppression of forming I$_3^-$ (Rxn. 3). By far, the processes of how I$_2$ can convert to I$^-$ when exposed to Br-containing perovskite is explained.

2.3. Comparison of I$_2$ Induced I-Rich Phase Formation in the Dark and under Illumination

So far, we have only investigated the effects of I$_2$ exposure in the dark. The notorious I-rich phase formation happens in lead mixed I-Br perovskites under illumination. Illumination may not only induce I$_2$ formation (Figures 1a,b), but also alters the kinetics of the reactions between I$_2$ and the perovskite. The pure-Br (Cs$_{0.17}$FA$_{0.83}$PbBr$_3$) rather than the mixed I-Br (Cs$_{0.17}$FA$_{0.83}$PbI$_{1.5}$Br$_{1.5}$) perovskite is used for the investigation of I$_2$ exposure under illumination, to avoid the influence of I$_2$ inherently formed in the perovskite. The PL and UV–Vis absorption spectra of the perovskite after I$_2$ exposure in the dark and under illumination were both collected for comparison and are shown in **Figure 3**. In the dark, an additional emission peaking at 705 nm shows up in the PL of Cs$_{0.17}$FA$_{0.83}$PbBr$_3$ after 20 min of I$_2$ exposure, which further redshifts to 758 nm after 40 min exposure (Figure 3b). The absorption of the Cs$_{0.17}$FA$_{0.83}$PbBr$_3$ perovskite upon I$_2$ exposure increases slightly in the longer wavelength range and mainly below 700 nm (Figure 3c). Meanwhile, though the I-rich phase with absorption edge at ≈758 nm cannot be detected by UV–Vis absorption spectroscopy (Figure 3c), the charge carriers can still be funneled to this phase and recombine radiatively, which indicates the I-rich phase with lowest bandgap can redshift the PL strongly even with a very minor quantity. Under illumination with a 405 nm diode laser with an intensity of 50 mW cm^{-2} (Figure 3d), the PL emission of I-rich phase shows more significant redshift than in the dark, to 763 and 774 nm after 20 and 40 min of I$_2$ exposure, respectively (Figure 3e). By monitoring the PL behavior within the first 90 s under illumination and I$_2$ exposure, we find that the PL maxima of the I-rich phase reaches 690 nm within 30 s, and then redshift rapidly to 756 nm within 90 s (Figure S5, Supporting Information). Therefore, PL redshift of the I-rich phase is identical in trend but much more rapid under illumination when compared with the PL shift in the dark upon I$_2$ exposure (Figure 3b,e; Figure S5, Supporting Information). Meanwhile, the absorption increases more significantly at the longer wavelength upon I$_2$ exposure under illumination than in the dark, and the increase in the 700 to 800 nm range is clearly observed (Figure 3f). This indicates the faster formation rate of I-rich phase and thus the faster redshift of its PL in the Cs$_{0.17}$FA$_{0.83}$PbBr$_3$ perovskite under illumination than in the dark upon I$_2$ exposure (Figures 3b,e; and Figure S5, Supporting Information). We have shown that the Br$^-$ binding strength in the chemical environment defines the formation rate of I$^-$ (through Rxns. 1–2) and thus I-rich phase (Figure 2; Figure S3, Supporting Information) upon I$_2$ exposure. It is expected that the bond of Br$^-$ to the lattice is weakened when the perovskite is under photo-excitation, as the electron is promoted from the valence band, contributed by the mixing of the halide-lead orbitals, to the conduction band, contributed only
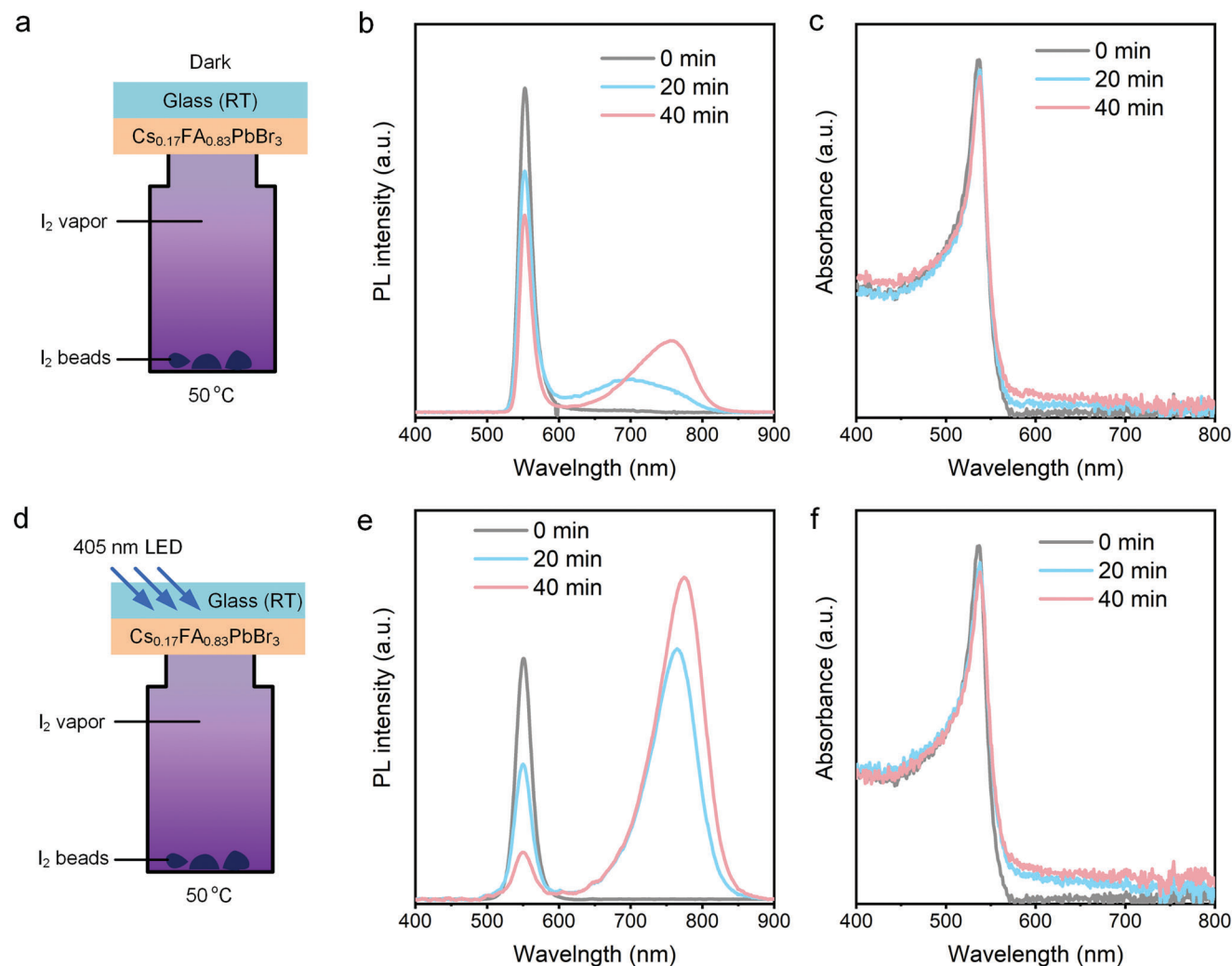
Figure 3. a) Schematic of I_2 exposure on the $Cs_{0.17}FA_{0.83}PbBr_3$ perovskite thin film in the dark. Evolution of b) PL and c) UV–Vis absorption of the $Cs_{0.17}FA_{0.83}PbBr_3$ perovskite thin film upon I_2 exposure in the dark. d) Schematic of I_2 exposure on the $Cs_{0.17}FA_{0.83}PbBr_3$ perovskite thin film under illumination. Evolution of e) PL and f) UV–Vis absorption of the $Cs_{0.17}FA_{0.83}PbBr_3$ perovskite thin film upon I_2 exposure under illumination.

by the lead orbitals.[31] The reduced binding strength of Br^- may also increase concentration of Br^- interstitials due to the reduced energy barrier of forming the Frenkel pair. Therefore, halide exchange through Rxn. 2 is increased, either by reacting with Br^- from the lattice (with weakened binding strength) or by reacting with interstitial Br^- (free of binding) at a higher concentration. Therefore, it is expected to have an overall higher I^- concentration in the perovskite lattice upon I_2 exposure under illumination than in the dark as reflected by PL and UV–Vis absorption results (Figure 3).

2.4. Mechanism behind Photo-Induced I-Rich Phase Formation in Mixed I-Br Perovskites

Based on the investigation of the effects of I_2 exposure by using the mixed I-Br and pure-Br perovskites, we elucidate the possible processes behind the widely known photo-induced I-rich phase formation in mixed I-Br perovskites.[4] It has been reported that PL emission at a specific wavelength is commonly observed when the mixed I-Br perovskite is under illumination, which corresponds to a perovskite with a Br-fraction x of ≈0.2.[1b,4] Multiple strain-based models suggest that this is because of a halide phase segregation process complying with a phase diagram.[7a,8] However, Suchan and co-workers revealed recently that the formed I-rich phase does not show a specific Br-fraction through combined PL and XRD analysis.[32] Here, we monitored the PL evolution of the $Cs_{0.17}FA_{0.83}PbI_{1.5}Br_{1.5}$ thin film under continuous illumination of a 405 nm diode laser with an intensity ≈50 mw cm^{-2} over 120 min. At the initial stage of the PL evolution, it seems that the newly formed PL emission is at a specific wavelength (≈743 nm, **Figure 4**b) within a short period of 5 min. However, the newly emerged PL emission redshifts all the way to 780 nm (Figure 4b) which is close to that of $Cs_{0.17}FA_{0.83}PbI_3$ pure iodide perovskite at 786 nm (Figure S6, Supporting Information). This suggests an I-enrichment, other than a phase segregation process, is happening when the mixed halide perovskite is under continuous illumination. This is further confirmed by
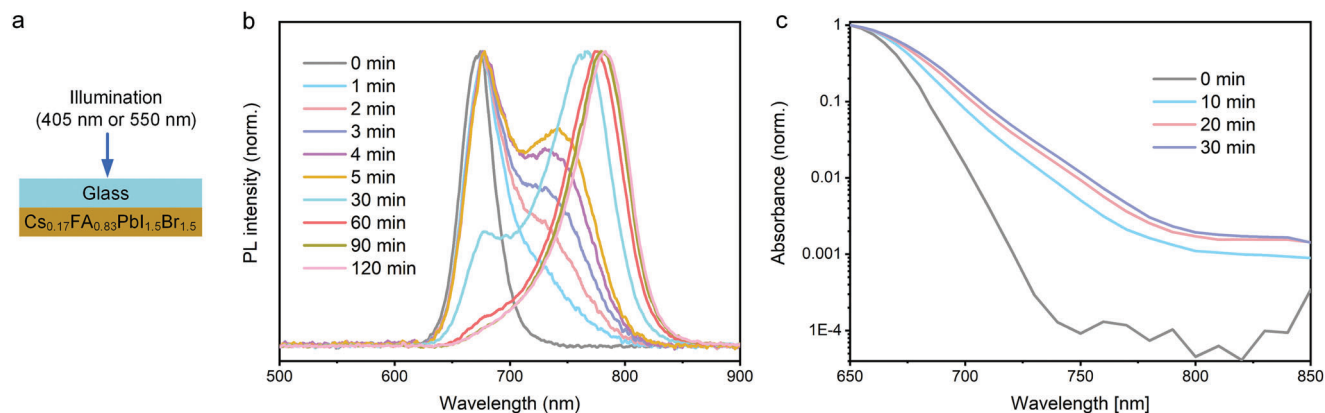
ADVANCED
SCIENCE NEWS

www.advancedsciencenews.com

ADVANCED
MATERIALS

www.advmat.de

Figure 4. a) Schematic of inducing the I-rich phase formation in the perovskite. For PL and PDS measurements, the light sources used are a 405 nm (50 mW cm^{-2}) and 550 nm (100 mW cm^{-2}) diode lasers, respectively. b) PL evolution of the $Cs_{0.17}FA_{0.83}PbI_{1.5}Br_{1.5}$ perovskite thin film under illumination over 120 min. c) Evolution of PDS spectrum of the $Cs_{0.17}FA_{0.83}PbI_{1.5}Br_{1.5}$ perovskite thin film under illumination over 30 min.

photothermal deflection spectroscopy (PDS), that during the illumination of the $Cs_{0.17}FA_{0.83}PbI_{1.5}Br_{1.5}$ perovskite over 30 min with a 550 nm diode laser (100 mW cm^{-2}), the I-rich phase with the lowest bandgap always has the lowest quantity (Figure 4c), which does not support the preferential formation of an I-rich phase with a specific Br-fraction. A recent study from Ridzonova and co-workers demonstrated identical behaviors of PL and formation of I-rich phase in the mixed I-Br perovskite.[33]

Based on the results shown above, we propose the following mechanism behind the photo-induced I-rich phase formation. Under illumination, I_2 is first formed in the mixed I-Br perovskite (Figures 1a,b), which is then expulsed to the grain boundary due the relief of the lattice strain.[19a,34] Considering the grain boundary is a relatively closed space, we estimated that I_2 can reach its saturated vapor pressure there within tens of seconds, based on the I_2 formation rate derived from Figure 1b and the volume of the grain boundary estimated from SEM image of the perovskite (Figure S7, see Supporting Information for the detail of the estimation). I_2 can then interact with Br$^-$ at the grain surface to produce I$^-$ following Rxns. 1 and 2, which further enters the perovskite lattice and causes the formation of I-rich phase. The formation of I-rich phase has indeed been observed to initiate from the grain boundaries.[8,13c] As this is an I-enrichment process, the I-rich phase with higher I-concentration (lower bandgap) has slower rate to be formed, which causes a distribution of I-rich phase quantity from high to low following the decrease of bandgap (Figure 4c). However, the PL emission of I-rich phase is dominated by the one with the lowest bandgap due to the strong charge funneling, and this emission will redshift continuously toward that of the pure iodide perovskite upon illumination (Figure 4b), as the I-content in the I-rich phase with the lowest bandgap will be enriched toward that of pure iodide perovskite.

Importantly, please note that photo-induced I-rich phase formation was initially reported as reversible in mixed I-Br perovskites.[4] Also after being tranferred to a N_2 (I_2-free) environment, the PL of the I_2-treated $Cs_{0.17}FA_{0.83}PbI_{1.5}Br_{1.5}$ thin film slowly (over several hours Figure S15a, Supporting Information) goes back to the original peak at higher energy. This is possible due to the reversal of Rxns. 1 and 2 once I_2 supply stops. For the

photoaged mixed I-Br perovskites being stored in the dark, the photogeneration of I_2 stops which may also cause the reversal of Rxns. 1 and 2 and the release of I_2 to the grain boundary due to the decomposition of I_2Br^-. Then I_2 may react with Pb^0 (another byproduct of photodecomposition) to form perovskite again which could cause the reversal of halide segregation.[18b] However, Knight and co-workers found that reversibility highly depends on the photo-aging environment and history of the mixed I-Br perovskite.[13e] Specifically, halide segregation is mostly reversible when the film is encapsulated with a PMMA layer, while it is apparently not reversible in vacuum.[13e] Moreover, the reversibility is reduced with more cycles of light illumination.[13e] These observations agree with a reversibility correlated with the probability of I_2 escaping the perovskite. The suppression of photo-induced halide segregation at elevated temperature up to 70 °C has been reported.[35] We found that the recovery of PL of the I_2-treated $Cs_{0.17}FA_{0.83}PbI_{1.5}Br_{1.5}$ thin film in a N_2 (I_2-free) environment is much faster at 70 °C than at 25 °C (Figure S15b, Supporting Information). The reversal of Rxns. 1 is accelerated significantly as the triple halide ion I_2Br^- is much less stable at 70 °C than at 25 °C (Figure S15c, Supporting Information), which possibly causes the much faster PL recovery at higher temperature (Figure S15b, Supporting Information). Therefore, when the perovskite is under illumination and heating (for example 70 °C), the photogenerated I_2 becomes less favorable to react with Br$^-$ to form I_2Br^- which possibly contributes to the suppressed photo-induced halide segregation at higher temperature.

It has been shown that the incorporation of Cs$^+$ can slow down the photo-induced I-rich phase formation.[1b] Here we prepared $CsPbI_{1.5}Br_{1.5}$ perovskite thin film, which shows a more stable PL emission than $Cs_{0.17}FA_{0.83}PbI_{1.5}Br_{1.5}$ under the same illumination (Figures 4b and 5a). We further fabricated $Cs_{0.17}FA_{0.83}PbI_{1.5}Br_{1.5}$ and $CsPbI_{1.5}Br_{1.5}$ perovskite solar cells in an *n-i-p* device architecture. The photovoltaic parameters recorded with simulated AM1.5G illumination and the external quantum efficiency (EQE) spectra are shown in Figures S8–11 (Supporting Information). The in situ PL measurements were conducted while devices were aged either under open-circuit condition or at a voltage bias of 0.80 times the maximum power point voltage (0.80 × V_{MPP}) to check for stability under

**ADVANCED
SCIENCE NEWS**

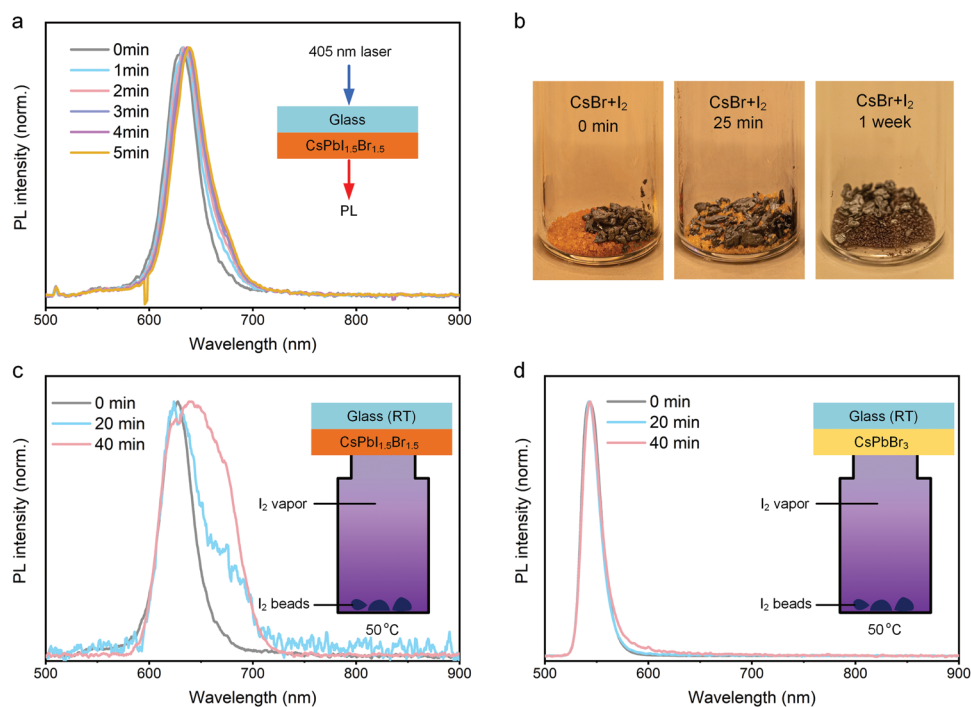www.advancedsciencenews.com

**ADVANCED
MATERIALS**

www.advmat.de

Figure 5. a) PL evolution of the $CsPbI_{1.5}Br_{1.5}$ perovskite thin film under the illumination of a 405 nm diode with an intensity of 50 mW cm^{-2}. b) The feasibility of the reaction in CsBr-I_2 mixture over a duration of 1 week. PL evolution of c) $CsPbI_{1.5}Br_{1.5}$ and d) $CsPbBr_3$ perovskite thin films upon I_2 exposure in the dark over 40 min.

representative operating conditions (Shown schematically in Figure S12a, Supporting Information). Under both aging conditions, the $CsPbI_{1.5}Br_{1.5}$ perovskite thin film shows better stability of the PL (Figures S12b–e, Supporting Information), and in general, of all figures of merit of the solar cell (Figure S13, Supporting Information) than the $Cs_{0.17}FA_{0.83}PbI_{1.5}Br_{1.5}$ counterpart I_2 formation in the mixed I-Br perovskite under illumination is the first key step to induce I-rich phase formation. We then checked the I_2 formation in the $CsPbI_{1.5}Br_{1.5}$ perovskite thin film following the same method used to check that in the $Cs_{0.17}FA_{0.83}PbI_{1.5}Br_{1.5}$ counterpart. It is found that the I_2 formation rate is identical in $CsPbI_{1.5}Br_{1.5}$ and $Cs_{0.17}FA_{0.83}PbI_{1.5}Br_{1.5}$ thin films under illumination (Figure S14, Supporting Information). Meanwhile, I_2 shows a higher barrier to react with Br$^-$ in the pure-Cs environment than in the FA-containing environment to form triple halide ion (Figures 2c; Figures S3 and S4, Supporting Information). Therefore, the possible reason that $CsPbI_{1.5}Br_{1.5}$ has a higher spectral stability than $Cs_{0.17}FA_{0.83}PbI_{1.5}Br_{1.5}$ is mainly due to the higher Br$^-$ binding strength and the suppressed production of I$^-$ and thus I-rich phase through Rxns. 1 and 2, when the I_2 supply is identical. Please note that the emergence of PL emission at longer wavelengths is still observable in $CsPbI_{1.5}Br_{1.5}$ perovskite under illumination (**Figure 5**a), which indicates the I-rich phase formation is not suppressed completely. This is possibly because the reaction between CsBr and I_2 can still happen but in a much slower rate, as after 1 week the CsBr-I_2 mixture shows the formation of dark-red compound (Figure 5b). Furthermore, we also exposed I_2 to $CsPbI_{1.5}Br_{1.5}$ and $CsPbBr_3$ thin films, and in both cases the emerging of PL emission at longer

wavelength are visible but are highly suppressed (Figure 5c,d) compared with the $Cs_{0.17}FA_{0.83}PbI_{1.5}Br_{1.5}$ and $Cs_{0.17}FA_{0.83}PbBr_3$ counterparts (Figures 1d and 3b), respectively. Meanwhile, it is found that mixed I-Br perovskites always show more significant PL redshift than pure-Br counterparts when exposed to I_2.

To clearly depict the impact of chemical composition on the stability of perovskites phases and the thermodynamics of I_2 incorporation, we carry out density functional theory (DFT) on $APbI_{3-x}Br_x$ compositions (A = FA, MA or Cs; x = 0, 1.5 and 3). We start by calculating the perovskite formation energy ($\Delta_f H$, **Table 1**) from precursors. For a fixed A-site cation, a progressive decrease in stability (more positive $\Delta_f H$) is reported by increasing the iodide content (Table 1), in agreement with reported experimental data.[36] For a fixed halide composition, an increase of stability (within the perovskite "black" phase, for tri-iodide samples) is observed moving from FA, MA, and Cs (Table 1), which is consistent with the decrease of the tolerance factor resulting from the smaller cation radius. An additional contribution to the stability of mixed halide (and in general of alloyed) perovskites comes from the entropy of mixing, which at 300 K accounts to a stabilization 0.05 eV per formula unit, see Table 1 and it further increases at higher temperature. Based on these observations and the data shown in Table 1, it is clear that the capability of an electron accepting I_2 molecule to perturb the pristine perovskite structure will be less effective when the iodide content in the perovskite is decreased, as well as when moving to Cs cation. It is significative to notice, looking at the same scenario from an electronic point of view, that the valence band of Cs halide perovskites is typically deeper than that of FA-based counterparts, due to octahedra

**ADVANCED
SCIENCE NEWS**

www.advancedsciencenews.com

**ADVANCED
MATERIALS**

www.advmat.de

Table 1. Formation energies of the investigated perovskites starting from precursors (Δ_fH). For mixed halide perovskites the Gibbs formation energies ($\Delta G = \Delta_f H - T\Delta S$) are reported in parenthesis by adding the mixing entropy times 300 K ($-T\Delta S = -0.05$ eV per f.u.) to Δ_fH. I_2 incorporation energy (**$\Delta(E)I_2$**) calculated as the sum of the defect formation energies of positive I_i^+ and negative I_i^- iodine interstitials calculated at the VBM of the perovskites in I-rich conditions. Please note that for the lead tri-iodide semiconductors, the formation energy and stability comparisons are done within the perovskite (black) phase.

Phase	Δ_fH [eV]	$\Delta(E)I_2$ [eV]
FAPbBr$_3$	−0.02	0.80
FAPbBr$_{5/3}$I$_{4/3}$	0.08 (0.03)	0.13
FAPbI$_3$	0.14	0.30
MAPbBr$_3$	−0.13	1.62
MAPbBr$_{1.5}$I$_{1.5}$	0.01 (−0.04)	1.01
MAPbI$_3$	0.01	0.86
CsPbBr$_3$	−0.31	1.40
CsPbBr$_{1.5}$I$_{1.5}$	−0.16 (−0.21)	0.96
CsPbI$_3$	−0.14	0.92

tilting, which can be read as better capability of Cs of keeping halogen electrons more bounded.[37]

As previously reported, a I_2 molecular is stable in a combination of a positive and a negative interstitials in the perovskite bulk according to reaction $I_2 = I_i^+ + I_i^-$.[38] To estimate the incorporation thermodynamics of I_2 in different perovskites, the defect formation energies (DFEs) of the I_i^+ and I_i^- interstitials was thus calculated and the structures are shown in Figure S16 (Supporting Information). By neglecting defect couple interactions, an estimate of the I_2 incorporation energy is obtained by summing the DFEs of the two interstitials. I_2 incorporation into the perovskite lattice is more favorable in full iodide than full bromide perovskites, by showing a monotonic trend moving between the two extrema, except for the mixed-halide FA perovskite. By comparing the different cations, $\Delta(E)I_2$ increases following the sequence of FA, MA, and Cs. Overall, the observed trend indicates that I_2 incorporation is more favorable in FA-based perovskites, which are the least stable composition examined here. Using cations with smaller radius (Cs$^+$) increases the lattice stability and reduces the tendency to incorporate the electron accepting I_2 molecule.

3. Conclusions

In summary, we demonstrated how I_2 formed through photo-carrier trappings at interstitial iodide defects can cause bandgap photo-instability in the mixed I-Br perovskite. Specifically, I_2 undergoes a redox process to react with Br$^-$ to form I_2Br$^-$ (I$^{\delta-}$-I$^{\delta+}$-Br$^{\delta-}$), whose negatively charge iodide (I$^{\delta-}$) can further exchange with another lattice Br$^-$ and leads to the formation of I-rich phase. Such a process is regulated by the binding strength of Br$^-$ in the perovskite. These findings allow to describe the process behind the photo-instability of mixed I-Br perovskites and rationalize a variety of experimental observation. For example, it has been re-

ported that monovalent cations of rubidium (Rb$^+$)[39] and potassium (K$^+$)[40] also help to suppress halide segregation. This observation also agrees with our model as Rb$^+$ and K$^+$ have smaller sizes and thus higher charge density than FA$^+$[26] and should have identical role as Cs$^+$ to increase the binding strength of Br$^-$ in the perovskite. We provide a new insight to rationalize the role of the chemical composition of the perovskite unit cell, which not only aims at the reduction of native defects causing I_2 formation, but also looks at the improvement of the binding strength of Br$^-$ by introducing cations with higher charge density in the perovskite.

4. Experimental Section

Substrate Cleaning: Fluorine-doped tin oxide (FTO)-coated glass was etched with zinc powder and 2 M aqueous HCl solution for electrode pattern. The FTO and glass substrates were washed with 2% Hellmanex in water, deionized water, iso-propanol, acetone, and iso-propanol subsequently in a sonication bath for 15 min.

For the solar cells used for the in situ PL and *J-V* measurement at a voltage bias of $0.8 \times V_{MPP}$, patterned indium tin oxide (ITO) covered glass substrates were used. The substrates were cleaned by sonicating in an acetone bath, scrubbing and sonicating in an aqueous solution of dodecyl sodium sulphate (Acros, 99%). After rinsing in deionized water, substrates were sonicated in 2-propanol. The substrates were dried and treated with UV-ozone for 30 min.

Preparation of Electron Transporting Layer: The SnO$_2$ colloid precursor was obtained from Alfa Aesar (tin(IV) oxide, 15% in H$_2$O colloidal dispersion). Before use, the SnO$_2$ colloid precursor was mixed with water in a volume ration of 1:5.67. The FTO substrates were treated by O$_2$ plasma cleaning for 10 min before depositing of SnO$_2$. The diluted SnO$_2$ colloid solution was spin coated onto FTO substrates at 3000 rpm for 30 s, and then baked on a hotplate in ambient air (humidity ≈70% RH, temperature ≈22 °C) at 120 °C for 10 min, followed by 30 min at 180 °C. After annealing, the hotplate was switched off, and the FTO substrates were allowed to cool down to room temperature naturally. Subsequently, the substrates were treated by UV-ozone for 15 min and then transferred to a N$_2$ filled glovebox.

For the solar cells used for the in situ PL and *J-V* measurement at a voltage bias of $0.8 \times V_{MPP}$, the electron transporting layer is prepared as follows. The SnO$_2$ colloid precursor was obtained from Alfa Aesar (tin(IV) oxide, 15wt.% in H$_2$O colloidal dispersion). Before use, the SnO$_2$ colloid precursor was mixed with water in a volume ratio of 1:5. The SnO$_2$ dispersion was spin-coated onto the ITO/glass substrates at 2800 rpm (with a 2000 rpm^{-1} s acceleration) for 60 s and dried at 150 °C for 30 min in an ambient atmosphere. The SnO$_2$ film was treated with UV-ozone for 10 min and then quickly transferred into a nitrogen-filled glovebox. A layer of PCBA was deposited before depositing perovskite. The [6,6]-phenyl-C$_{61}$-butyric acid (PCBA), dissolved in 1,2-dichlorobenzene (DCB, Sigma-Aldrich, anhydrous 99%) at 0.1–0.2 mg mL^{-1} and stirred at 60 °C, was spin-coated onto the SnO$_2$ substrate at 2000 rpm (with a 3000 rpm $^{-1}$ s acceleration) for 30 s.

Material Fabrication: The precursor of Cs$_{0.17}$FA$_{0.83}$PbI$_{1.5}$Br$_{1.5}$ perovskite was prepared by mixing 0.17 M CsI (Alfa- Aesar 99.999%), 0.83 M FAI (Great Solar), 0.25 M PbI$_2$ (TCI, 99.99%) and 0.75 M PbBr$_2$ (TCI, >98%) in anhydrous DMF: DMSO 4:1 (v:v) and stirred overnight. The precursor of Cs$_{0.17}$FA$_{0.83}$PbBr$_3$ was prepared by mixing 0.085 M CsBr (Alfa-Aesar, 99.999%), 0.415 M FABr (Great Solar) and 0.5 M PbBr$_2$ (TCI, >98%) in anhydrous DMF: DMSO 4:1 (v:v) and stirred overnight. The precursor of FAPbBr$_3$ was prepared by mixing 0.5 M FABr (Great Solar) and 0.5 M PbBr$_2$ (TCI, >98%) in anhydrous DMF: DMSO 4:1 (v:v) and stirred overnight. The precursor of CsPbI$_{1.5}$Br$_{1.5}$ was prepared by mixing 1 M CsI (Alfa- Aesar, 99.999%), 0.25 M PbI$_2$ (TCI, 99.99%) and 0.75 M PbBr$_2$ (TCI, >98%) in anhydrous DMSO. The precursor of CsPbBr$_3$ was prepared by mixing 0.5 M CsBr (Alfa-Aesar, 99.999%) and 0.5 M PbBr$_2$ (TCI, >98%) in anhydrous DMSO. The thin films were deposited by spin-coating on the glass

**ADVANCED
SCIENCE NEWS**

www.advancedsciencenews.com

**ADVANCED
MATERIALS**

www.advmat.de

substrates in a two-step procedure at 1000 rpm and 5000 rpm for 10 s and 40 s respectively. During the second step, 120 µL of chlorobenzene was casted onto the substrates 10 s before the ending of the second spinning step. The films were placed on a hotplate at 100 °C for 30 min. The perovskite powders were obtained by scratching off the thin films from the glass.

For the $CsPbI_{1.5}Br_{1.5}$ solar cells used for the in situ PL and J-V measurement at a voltage bias of $0.8 \times V_{MPP}$, the precursor was prepared by mixing 0.87 M CsI (Sigma-Aldrich, 99.999%), 0.22 M PbI_2 (TCI, 99.99%) and 0.65 M $PbBr_2$ (TCI, >98.0%) in anhydrous DMF:DMSO 1:1.89 (v:v). The precursor was spin-coated onto the glass substrates in a two-step procedure at 600 rpm and 4000 rpm for 5 s and 30 s, respectively. During the second step, 200 µL of methyl acetate was cast onto the substrates 10 s before the ending of the second spinning step. The films were subsequently placed on a hotplate at 35 °C for 5 min, at 120 °C for 10 min, and at 160 °C for 5 min. For the $Cs_{0.17}FA_{0.83}PbI_{1.5}Br_{1.5}$ solar cells used for the in situ PL and J-V measurement at a voltage bias of $0.8 \times V_{MPP}$, the precursor and the spin-coating procedure was the same as described above, except for the use of ethyl acetate instead of chlorobenzene as antisolvent. The preparation of perovskite thin films for solar cells was performed in a N_2-purged glovebox (H_2O : <10 ppm and O_2 < 5 ppm).

Preparation of Hole Transport Layer and Au Electrode: The hole-transport layer precursor was prepared by dissolving 72.3 mg spiro-MeOTAD (Luminescence Technology, 99.9%), 28 µL 4-tert-butylpyridine (Sigma-Aldrich, 96%) and 17.5 µL bis(trifluoromethane)sulfonimide lithium salt (Sigma-Aldrich) solution (520 mg Li-TFSI in 1 mL acetonitrile) in 1 mL chlorobenzene. The precursor was then spin-coated on the perovskite layer at 4000 rpm for 30 s. The deposition of the hole transport layer was in a glovebox. The solar cells were then transferred to a box with dry air (humidity lower than 20% RH) for oxidation for 16 h. Finally, a 100 nm Au electrode layer was deposited under a vacuum of $<1\times10^{-4}$ Pa with a rate of 0.1 nm^{-1} s. The preparation of the Au electrode was performed in a N_2-purged glovebox.

For the solar cells used for the in situ PL and J-V measurement at a voltage bias of $0.8 \times V_{MPP}$, the spiro-OMeTAD (80 mg) (Lumtec, 99.5%) was dissolved in chlorobenzene (1 mL) with 4-tert-butylpyridine (28.5 µL) (Sigma-Aldrich, 99.5%) and bis(trifluoromethylsulfonyl)amine lithium salt (16.6 µL) (Sigma-Aldrich, 99.95% trace metal basis) of a solution (500 mg mL^{-1}) in acetonitrile (Sigma-Aldrich, anhydrous 99.8%) at 60 °C. Before the deposition, tris(2-(1H-pyrazol-1-yl)-4-tert-butylpyridine)cobalt(III) tri[bis(trifluoromethane)sulfonimide] (20 µL) (Greatcell Solar) of a solution (500 mg mL^{-1}) in acetonitrile was added to the Spiro-OMeTAD solution. The chemically doped Spiro-OMeTAD solution was dynamically spin-coated onto the perovskite layer at 2000 rpm (with a 20 000 rpm^{-1} s acceleration) for 50 s. The sample was then exposed to dry air for 20 min, before being transferred back into the glovebox. Finally, MoO_3 (10 nm) and Au (100 nm) were sequentially evaporated under high vacuum ($\approx 3 \times 10^{-7}$ mbar).

I_2 Vapor Exposure to Perovskite Films: The I_2-vapor exposure experiments were done in a N_2-filled glove box (H_2O : <10 ppm and O_2 < 5 ppm) under dark or illumination. The dark is realized by covering the vial loaded with perovskite samples with Al foils. The illumination is provided by a 405 nm diode laser with an intensity of 50 mW m^{-2}. 20 mg of I_2 beads (Sigma-Aldrich, 99.99%) was placed in a vial with a height of 10 cm and a diameter 1.5 cm, which was placed on a hot plate. To expose the sample to I_2 vapor, we heated the vial loaded with I_2 pellet at 50 °C, while covering the vial with perovskite sample. Since the vial is 10 cm long, we can realize heating only the I_2 pellet to produce I_2 vapor while keeping the perovskite sample at an ambient temperature of 22 °C. This means the sample suffered only from I_2-vapor exposure, and the possible effect due to sample heating (for example, decomposition) was minimized.

Triple Halide Ion Formation: The mixture of CsBr (Alfa-Aesar, 99.999%), FABr (Great Solar) and I_2 (Sigma-Aldrich, 99.99%) was prepared by mixing them in a mole ratio of 0.17: 0.83: 1. The mixture of CsBr (Alfa-Aesar, 99.999%) and I_2 (Sigma-Aldrich, 99.99%) is prepared by mixing them in a mole ratio of 1: 1. The mixture of FABr (Great Solar) and I_2 (Sigma-Aldrich, 99.99%) was prepared by mixing them in a mole ratio of

1: 1. The mixture of FAI (Great Solar) and I_2 (Sigma-Aldrich, 99.99%) was prepared by mixing them in a mole ratio of 1: 1. The mixture of FABr (Great Solar) and IBr (Sigma-Aldrich, >98%) was prepared by mixing them in a mole ratio of 1: 1. The mixture of $FAPbBr_3$ powder and I_2 (Sigma-Aldrich, 99.99%) were prepared by mixing them in a mole ratio of 1: 1. The preparation of the mixture was conducted in a glovebox filled with N_2. The mixture of $CsPbBr_3$ powder and I_2 (Sigma-Aldrich, 99.99%) were prepared by mixing them in a mole ratio of 1: 1. The preparation of the mixture was conducted in a glovebox filled with N_2.

I_2 Formation Test: Each of the perovskite thin film on glass substrate was sealed in an 8 mL vial filled with 6 mL anhydrous toluene. The vial was further sealed with a plastic bag in N_2-filled glovebox. The vial was put under simulated 1 sun illumination provided by a white LED array over 1 to 3 h at 30 °C.

Measurement and Characterizations: The X-ray diffraction (XRD) patterns of the samples were recorded using a Bruker D8 Advance equipped with a Cu $K\alpha 1$ ($\lambda = 1.544060$ Å) anode, operating at 40 kV and 40 mA. UV–Vis absorption spectra were recorded with a UV–Vis Varian Cary 5000. PL measurements were conducted by using a 405 nm laser with an intensity of 50 mW cm^{-2}. The PL was acquired with a Maya 2000 pro spectrometer from Ocean Optics. Raman spectra (Renishaw) were measured by using a 785 nm laser. The light source was particularly selected to avoid the PL signal and photochemical degradation that were known to be an issue when performing Raman spectroscopy on halide perovskites. X-ray Photoelectron Spectroscopy (XPS) analyses were performed to evaluate the chemical composition of the materials under investigation. The measurements were carried out with a Kratos Axis Ultra^{DLD} spectrometer. High-resolution spectra were acquired at a pass energy of 10 eV using a monochromatic Al $K\alpha$ source (15 kV, 20 mA), over the binding energy regions typical for Cs 3d, I 3d, N 1s, C 1s, Pb 4f, and Br 3d peaks.

The current density – voltage (J-V) characteristics of the solar cells were measured with a computer-controlled Keithley 2420 source meter in the air with device encapsulation. The simulated Air Mass 1.5 Global (AM 1.5G) irradiance was provided with a class AAA Newport solar simulator. The light intensity was calibrated with a silicon reference cell with a spectral mismatch factor of 0.99. The active area of the complete device was determined by an illumination-shadowing mask which is 0.0935 cm^2. For the J-V measurement, the scan rate was 0.05 V s^{-1} for the slow scan. The forward scan started from 0 V (the short circuit condition) to 1.4 V, while the reverse scan was from 1.4 to 0 V. Preconditional stress was not done for PV measurements.

For the solar cells used for the in situ PL and J-V measurement at a voltage bias of $0.8 \times V_{MPP}$, J-V characteristics were measured in the glovebox by a Keithley 2400 source measure unit (SMU). A tungsten-halogen lamp filtered by a Schott GG385 UV filter and a Hoya LB120 daylight filter was used to simulate AM1.5G 100 mW cm^{-2} solar light. A black shadow mask with an aperture area of 0.0676 or 0.1296 cm^2 was used to define the illuminated cell area. EQE spectra were recorded with a home-built set up using light of a tungsten-halogen lamp (Philips focusline, 50 W) that was modulated by a mechanical chopper (Stanford Research, SR 540) before passing into a monochromator (Oriel, Cornerstone 130). The spectral response of the device was recorded as a voltage from a pre-amplifier (Stanford Research, SR 570) using a lock-in amplifier (Stanford Research, SR 830), and was calibrated by a reference silicon cell. A green diode laser (530 nm, Thorlabs M530L3, driven by a DC4104 driver) was used as a light bias to provide the solar cell with approximately one sun illumination intensity during the measurement.

To record PL and V_{OC} data simultaneously during continuous illumination (405 nm, 50 mW cm^{-2}) in open circuit condition, the solar cells are mounted in a Arkeo stability platform (Cicci Research, Italy) with N_2 flow (temperature ≈27 °C). All the cells were encapsulated before stability test.

To record PL and J-V data simultaneously during continuous illumination, the solar cells were mounted in a custom-built holder to maintain an inert environment. The device area was defined by a shadow mask (0.16 cm^2 aperture) and the cell was connected to a Keithley 2400 source measure unit (SMU). A 405 nm diode laser (Thorlabs M405L4 diode laser driven by Thorlabs DC4104 driver) was used to illuminate the sample at an intensity determined by comparing the current output to the short-

circuit current density measured under AM1.5G 1-Sun illumination (circa 50 mW m^{-2}). The photoluminescence light (filtered by a 455 nm long pass filter) was focused on an optical fiber and recorded using a spectrometer (Avantes Avaspec – 2048×14). The SMU and spectrometer were operated on a custom-built LabVIEW code. Reverse and forward voltage scans were sequentially conducted between +1.25 and −0.2 V at a rate of 0.12 V s^{-1}, followed by acquisition of a photoluminescence spectrum from the active area of the solar cell while the cell was held in open-circuit. In between measurements, the cells were continuously illuminated and held below the maximum power point voltage (V_{MPP}) at $0.8 \times V_{MPP}$, where V_{MPP} was determined from the reverse current density – voltage scan under AM1.5G illumination. The cycle (J-V scan, PL measurement, delay) was repeated for a pre-set duration. The measurements were conducted at room temperature without active temperature control. The V_{MPP} was ≈0.8 V for CsFA-perovskite and ≈0.9 V for Cs-perovskite. By going to $0.8 \times V_{MPP}$, it was ensured that charges will be extracted also when the V_{MPP} would be slightly reduced during the illumination. Figure S14 (Supporting Information) shows that at 0.8×0.8 V = 0.64 V (for CsFA) and 0.8×0.9 V = 0.72 V (for Cs) we remain in the part of the J-V curve where photocurrent changes slightly with a small offset from V_{MPP}. Hence we could be sure that we extracted the carriers.

Computational Detail: DFT calculations were carried out in periodic boundary conditions by using the Quantum Espresso simulation package.[41] The equilibrium structures of the different phases were found by relaxing both ion positions and cell parameters. Specifically, starting from the experimental structures of the full bromide perovskites (FAPbBr$_3$ trigonal,[42] MAPbBr$_3$ tetragonal,[43] CsPbBr$_3$ orthorhombic[44]), bromide ions were progressively substituted by iodides in order to form the mixed and full iodide perovskites. In all cases full relaxations of ion positions and cell parameters were performed. DFT calculations were conducted by using the Perdew-Burke-Ernzherof (PBE) functional[45] and by including DFTD3 dispersion corrections.[46] Norm-conserving pseudopotentials[47] (I 5s, 5p; Br 4s, 4p; N and C 2s, 2p; H 1s; Pb 5d, 6s, 6p shells explicitly included) with a cutoff of 60 Ry on the wavefunctions and converged k-point grids were used.

Interstitial iodines have been simulated in the 2×2×2 supercells of the optimized phases with the same computational setup described above and by sampling the Brillouin zone (BZ) at the Γ point. Relaxation of defect structures was performed by fixing cell parameters to the optimized values. DFEs and TILs were calculated according to the expressions[48]:

$$DFE \; \left[I_i^q\right] = E\left[I_i^q\right] - E[perf] - \mu_I + q\left(\varepsilon_{VB} + \varepsilon_F\right) + E_{corr}^q \qquad (5)$$

$$\varepsilon\left(q/q'\right) = \frac{E\left[I_i^q\right] - E\left[I_i^{q'}\right]}{q' - q} + \frac{E_{corr}^q - E_{corr}^{q'}}{q' - q} - \varepsilon_{VB} \qquad (6)$$

where the term $E[I_i^q]$ is the energy of the supercell with interstitial in charge state q, $E(perf)$ is the energy of the perfect supercell, μ_I is the chemical potentials of iodine $\mu(I) = \frac{1}{2}\mu(I_2\text{-solid})$, ε_{VB} is the valence band energy, ε_F and E_q^{corr} the Fermi level of the system and corrections due to periodic charges. Makov-Payne correction terms were applied considering a mean static dielectric constants $\varepsilon_0 = 22$, estimated by averaging the values for the pure bromide and iodide phases.

Supporting Information

Supporting Information is available from the Wiley Online Library or from the author.

Acknowledgements

Conflict of Interest

The authors declare no conflict of interest.

Data Availability Statement

The data that support the findings of this study are available from the corresponding author upon reasonable request.

Keywords

[1] a) J. H. Noh, S. H. Im, J. H. Heo, T. N. Mandal, S. I.l Seok, *Nano Lett.* **2013**, *13*, 1764; b) D. P. Mcmeekin, G. Sadoughi, W. Rehman, G. E. Eperon, M. Saliba, M. T. Hörantner, A. Haghighirad, N. Sakai, L. Korte, B. Rech, M. B. Johnston, L. M. Herz, H. J. Snaith, *Science* **2016**, *351*, 151; c) A. Sadhanala, S. Ahmad, B. Zhao, N. Giesbrecht, P. M. Pearce, F. Deschler, R. L. Z. Hoye, K. C. Gödel, T. Bein, P. Docampo, S. E. Dutton, M. F. L. De Volder, R. H. Friend, *Nano Lett.* **2015**, *15*, 6095.

[2] M. T. Hörantner, T. Leijtens, M. E. Ziffer, G. E. Eperon, M. G. Christoforo, M. D. Mcgehee, H. J. Snaith, *ACS Energy Lett.* **2017**, *2*, 2506.

[3] S. Adjokatse, H.-H. Fang, M. Loi, *Mater. Today* **2017**, *20*, 413.

[4] E. T. Hoke, D. J. Slotcavage, E. R. Dohner, A. R. Bowring, H. I. Karunadasa, M. D. Mcgehee, *Chem. Sci.* **2015**, *6*, 613.

[5] a) A. J. Knight, J. B. Patel, H. J. Snaith, M. B. Johnston, L. M. Herz, *Adv. Energy Mater.* **2020**, *10*, 1903488; b) S. Mahesh, J. M. Ball, R. D. J. Oliver, D. P. McMeekin, P. K. Nayak, M. B. Johnston, H. J. Snaith, *Energy Environ. Sci.* **2020**, *13*, 258.

[6] L. Gil-Escrig, A. Miquel-Sempere, M. Sessolo, H. J. Bolink, *J. Phys. Chem. Lett.* **2015**, *6*, 3743.

[7] a) F. Brivio, C. Caetano, A. Walsh, *J. Phys. Chem. Lett.* **2016**, *7*, 1083; b) Y. Zhao, P. Miao, J. Elia, H. Hu, X. Wang, T. Heumueller, Y.i Hou, G. J. Matt, A. Osvet, Y.u-T. Chen, M. Tarragó, D. De Ligny, T. Przybilla, P. Denninger, J. Will, J. Zhang, X. Tang, N. Li, C. He, A. Pan, A. J. Meixner, E. Spiecker, D. Zhang, C. J. Brabec, *Nat. Commun.* **2020**, *11*, 6328.

[8] C. G. Bischak, C. L. Hetherington, H. Wu, S. Aloni, D. F. Ogletree, D. T. Limmer, N. S. Ginsberg, *Nano Lett.* **2017**, *17*, 1028.

[9] T. Zhu, S. Teale, L. Grater, E. S. Vasileiadou, J. Sharir-Smith, B. Chen, M. G. Kanatzidis, E. H. Sargent, arXiv preprint arXiv:2301.12627 **2023**.

[10] a) S. Draguta, O. Sharia, S. J. Yoon, M. C. Brennan, Y. V. Morozov, J. S. Manser, P. V. Kamat, W. F. Schneider, M. Kuno, *Nat. Commun.* **2017**, *8*, 200; b) R. E. Beal, D. J. Slotcavage, T. Leijtens, A. R. Bowring, R. A. Belisle, W. H. Nguyen, G. F. Burkhard, E. T. Hoke, M. D. Mcgehee, *J. Phys. Chem. Lett.* **2016**, *7*, 746.

[11] T. W. J. Van De Goor, Y. Liu, S. Feldmann, S. A. Bourelle, T. Neumann, T. Winkler, N. D. Kelly, C. Liu, M. A. Jones, S. P. Emge, R. H. Friend, B. Monserrat, F. Deschler, S. E. Dutton, *J. Phys. Chem. C* **2021**, *125*, 15025.

[12] a) I. M. Pavlovetc, A. Ruth, I. Gushchina, L. Ngo, S. Zhang, Z. Zhang, M. Kuno, *ACS Energy Lett.* **2021**, *6*, 2064; b) Z. Chen, G. Brocks, S. Tao, P. A. Bobbert, *Nat. Commun.* **2021**, *12*, 2687.

[13] a) R. A. Belisle, K. A. Bush, L. Bertoluzzi, A. Gold-Parker, M. F. Toney, M. D. Mcgehee, *ACS Energy Lett.* **2018**, *3*, 2694; b) Y. Lin, B.o Chen, Y. Fang, J. Zhao, C. Bao, Z. Yu, Y. Deng, P. N. Rudd, Y. Yan, Y. Yuan, J. Huang, *Nat. Commun.* **2018**, *9*, 4981; c) X. Tang, M. Van Den Berg, E. Gu, A. Horneber, G. J. Matt, A. Osvet, A. J. Meixner, D. Zhang, C. J. Brabec, *Nano Lett.* **2018**, *18*, 2172; d) W. Fan, Y. Shi, T. Shi, S. Chu, W. Chen, K. O. Ighodalo, J. Zhao, X. Li, Z. Xiao, *ACS Energy Lett.* **2019**, *4*, 2052; e) A. J. Knight, A. D. Wright, J. B. Patel, D. P. Mcmeekin, H. J. Snaith, M. B. Johnston, L. M. Herz, *ACS Energy Lett.* **2019**, *4*, 75; f) H. Zhang, X.u Fu, Y. Tang, H. Wang, C. Zhang, W. W. Yu, X. Wang, Y.u Zhang, M. Xiao, *Nat. Commun.* **2019**, *10*, 1088; g) J. T. Dubose, P. V. Kamat, *Acc. Mater. Res.* **2022**, *3*, 761.

[14] A. J. Barker, A. Sadhanala, F. Deschler, M. Gandini, S. P. Senanayak, P. M. Pearce, E. Mosconi, A. J. Pearson, Y. Wu, A. R. Srimath Kandada, T. Leijtens, F. De Angelis, S. E. Dutton, A. Petrozza, R. H. Friend, *ACS Energy Lett.* **2017**, *2*, 1416.

[15] a) S. J. Yoon, M. Kuno, P. V. Kamat, *ACS Energy Lett.* **2017**, *2*, 1507; b) A. Ruth, M. C. Brennan, S. Draguta, Y. V. Morozov, M. Zhukovskyi, B. Janko, P. Zapol, M. Kuno, *ACS Energy Lett.* **2018**, *3*, 2321; c) Y. Zhou, I. Poli, D. Meggiolaro, F. De Angelis, A. Petrozza, *Nat. Rev. Mater.* **2021**, *6*, 986.

[16] a) D. Barboni, R. A. De Souza, *Energy Environ. Sci.* **2018**, *11*, 3266; b) G. Y. Kim, A. Senocrate, T.-Y. Yang, G. Gregori, M. Grätzel, J. Maier, *Nat. Mater.* **2018**, *17*, 445.

[17] G. Y. Kim, A. Senocrate, Y.-R. Wang, D. Moia, J. Maier, *Angew. Chem., Int. Ed.* **2021**, *60*, 820.

[18] a) R. A. Kerner, Z. Xu, B. W. Larson, B. P. Rand, *Joule* **2021**, *5*, 2273; b) L. A. Frolova, S. Y. Luchkin, Y. Lekina, L. G. Gutsev, S. A. Tsarev, I. S. Zhidkov, E. Z. Kurmaev, Z.e X. Shen, K. J. Stevenson, S. M. Aldoshin, P. A. Troshin, *Adv. Energy Mater.* **2021**, *11*, 2002934; c) G. F. Samu, Á. Balog, F. De Angelis, D. Meggiolaro, P. V. Kamat, C. Janáky, *J. Am. Chem. Soc.* **2019**, *141*, 10812.

[19] a) S. G. Motti, D. Meggiolaro, A. J. Barker, E. Mosconi, C. A. R. Perini, J. M. Ball, M. Gandini, M. Kim, F. De Angelis, A. Petrozza, *Nat. Photonics* **2019**, *13*, 532; b) S. Wang, Y. Jiang, E. J. Juarez-Perez, L. K. Ono, Y. Qi, *Nat. Energy* **2017**, *2*, 16195; c) Y.-H. Lin, N. Sakai, P. Da, J. Wu, H. C. Sansom, A. J. Ramadan, S. Mahesh, J. Liu, R. D. J. Oliver, J. Lim, L. Aspitarte, K. Sharma, P. K. Madhu, A. B. Morales-Vilches, P. K. Nayak, S. Bai, F. Gao, C. R. M. Grovenor, M. B. Johnston, J. G. Labram, J. R. Durrant, J. M. Ball, B. Wenger, B. Stannowski, H. J. Snaith, *Science* **2020**, *369*, 96.

[20] S. Martani, Y. Zhou, I. Poli, E. Aktas, D. Meggiolaro, J. Jiménez-López, E. L. Wong, L. Gregori, M. Prato, D. Di Girolamo, A. Abate, F. De Angelis, A. Petrozza, *ACS Energy Lett.* **2023**, *8*, 2801.

[21] Y. Zhou, Y.-H. Jia, H.-H. Fang, M. A. Loi, F.-Y. Xie, L. Gong, M.-C. Qin, X.-H. Lu, C.-P. Wong, N. Zhao, *Adv. Funct. Mater.* **2018**, *28*, 1803130.

[22] N. J. Jeon, J. H. Noh, Y. C. Kim, W. S. Yang, S. Ryu, S. I.l Seok, *Nat. Mater.* **2014**, *13*, 897.

[23] J. F. Moulder, *Physical Electronics* **1995**, 230.

[24] A. Abate, M. Brischetto, G. Cavallo, M. Lahtinen, P. Metrangolo, T. Pilati, S. Radice, G. Resnati, K. Rissanen, G. Terraneo, *Chem. Commun.* **2010**, *46*, 2724.

[25] Z. Lin, M. B. Hall, *Polyhedron* **1993**, *12*, 1499.

[26] L. E. Topol, *Inorg. Chem.* **1968**, *7*, 451.

[27] A. Van Den Bossche, E. De Witte, W. Dehaen, K. Binnemans, *Green Chem.* **2018**, *20*, 3327.

[28] J. Ibaceta-Jaña, R. Muydinov, P. Rosado, H. Mirhosseini, M. Chugh, O. Nazarenko, D. N. Dirin, D. Heinrich, M. R. Wagner, T. D. Kühne, B. Szyszka, M. V. Kovalenko, A. Hoffmann, *Phys. Chem. Chem. Phys.* **2020**, *22*, 5604.

[29] E. Eyal, A. Treinin, *J. Am. Chem. Soc.* **1964**, *86*, 4287.

[30] W. M. Latimer, *Soil Sci.* **1952**, *74*, 333.

[31] S. G. Motti, M. Gandini, A. J. Barker, J. M. Ball, A. R. Srimath Kandada, A. Petrozza, *ACS Energy Lett.* **2016**, *1*, 726.

[32] K. Suchan, J. Just, P. Beblo, C. Rehermann, A. Merdasa, R. Mainz, I. G. Scheblykin, E. Unger, *Adv. Funct. Mater.* **2022**, *33*, 2206047.

[33] K. Ridzonová, R. Grill, A. Peter Amalathas, B. Dzurňák, N. Neykova, L. S. Horák, P. Fiala, X. Y.u Chin, C. M. Wolff, Q. Jeangros, J. Holovský, *J. Mater. Chem. A* **2022**, *10*, 18928.

[34] D. Meggiolaro, S. G. Motti, E. Mosconi, A. J. Barker, J. Ball, C. Andrea Riccardo Perini, F. Deschler, A. Petrozza, F. De Angelis, *Energy Environ. Sci.* **2018**, *11*, 702.

[35] a) A. D. Wright, J. B. Patel, M. B. Johnston, L. M. Herz, *Adv. Mater.* **2023**, *35*, 2210834; b) P. Nandi, C. Giri, D. Swain, U. Manju, S. D. Mahanti, D. Topwal, *ACS Appl. Energy Mater.* **2018**, *1*, 3807.

[36] A. Senocrate, G. Y. Kim, M. Grätzel, J. Maier, *ACS Energy Lett.* **2019**, *4*, 2859.

[37] A. Amat, E. Mosconi, E. Ronca, C. Quarti, P. Umari, M.d. K. Nazeeruddin, M. Grätzel, F. De Angelis, *Nano Lett.* **2014**, *14*, 3608.

[38] D. Meggiolaro, E. Mosconi, F. De Angelis, *ACS Energy Lett.* **2018**, *3*, 447.

[39] C. Xu, X. Chen, S. Ma, M. Shi, S. Zhang, Z. Xiong, W. Fan, H. Si, H. Wu, Z. Zhang, Q. Liao, W. Yin, Z. Kang, Y. Zhang, *Adv. Mater.* **2022**, *34*, 2109998.

[40] M. Abdi-Jalebi, Z. Andaji-Garmaroudi, S. Cacovich, C. Stavrakas, B. Philippe, J. M. Richter, M. Alsari, E. P. Booker, E. M. Hutter, A. J. Pearson, S. Lilliu, T. J. Savenije, H. Rensmo, G. Divitini, C. Ducati, R. H. Friend, S. D. Stranks, *Nature* **2018**, *555*, 497.

[41] P. Giannozzi, S. Baroni, N. Bonini, M. Calandra, R. Car, C. Cavazzoni, D. Ceresoli, G. L. Chiarotti, M. Cococcioni, I. Dabo, A. Dal Corso, S. de Gironcoli, S. Fabris, G. Fratesi, R. Gebauer, U. Gerstmann, C. Gougoussis, A. Kokalj, M. Lazzeri, L. Martin-Samos, N. Marzari, F. Mauri, R. Mazzarello, S. Paolini, A. Pasquarello, L. Paulatto, C. Sbraccia, S. Scandolo, G. Sclauzero, A. P. Seitsonen, et al., *J. Phys.: Condens. Matter* **2009**, *21*, 395502.

[42] S. Govinda, B. P. Kore, D. Swain, A. Hossain, C. De, T. N. Guru Row, D. D. Sarma, *J. Phys. Chem. C* **2018**, *122*, 13758.

[43] A. Poglitsch, D. Weber, *J. Chem. Phys.* **1987**, *87*, 6373.

[44] C. C. Stoumpos, C. D. Malliakas, J. A. Peters, Z. Liu, M. Sebastian, J. Im, T. C. Chasapis, A. C. Wibowo, D. Y. Chung, A. J. Freeman, B. W. Wessels, M. G. Kanatzidis, *Cryst. Growth Des.* **2013**, *13*, 2722.

[45] J. P. Perdew, K. Burke, M. Ernzerhof, *Phys. Rev. Lett.* **1997**, *77*, 3865.

[46] S. Grimme, J. Antony, S. Ehrlich, H. Krieg, *J. Chem. Phys.* **2010**, *132*, 154104.

[47] a) D. R. Hamann, *Phys. Rev. B* **2017**, *88*, 085117; b) M. J. Van Setten, M. Giantomassi, E. Bousquet, M. J. Verstraete, D. R. Hamann, X. Gonze, G.-M. Rignanese, *Comput. Phys. Commun.* **2018**, *226*, 39.

[48] C. G. Van De Walle, J. Neugebauer, *J. Appl. Phys.* **2004**, *95*, 3851.